Catal Lett (2008) 121:311–318
DOI 10.1007/s10562-007-9340-1

Strong Size Effects in Supported Ionic Nanoparticles: Tailoring the Stability of NO_x Storage Catalysts

Aine Desikusumastuti · Mathias Laurin · Markus Happel · Zhihui Qin · Shamil Shaikhutdinov · Jörg Libuda

Received: 7 August 2007 / Accepted: 2 November 2007 / Published online: 20 November 2007

Abstract Based on a well-defined model-catalyst approach, we study the particle size dependent properties of NO_x storage materials. The single-crystal based model systems are prepared on an ordered Al_2O_3 film, on which BaO nanoparticles are grown under ultrahigh-vacuum (UVH) conditions. Particle size and density are characterized by scanning tunneling microscopy (STM). The interaction with NO_2 is probed by molecular beam (MB) methods in combination with time-resolved IR reflection absorption spectroscopy (TR-IRAS). It is found that both, the stability and the formation kinetics of alumina supported barium nitrate nanoparticles show a strong dependence on particle size. Very small BaO particles are rapidly converted into nitrates, however, the resulting aggregates exhibit a strongly reduced thermal stability. Surface and bulk nitrate and nitrate features are identified by means of vibrational spectroscopy. It is concluded that the size dependencies are related to the formation and decomposition of surface-related $BaNO_x$ species the decomposition temperature of which can be tuned over an exceptionally large temperature interval. It is suggested that the stability of these surface NO_x species is strongly modified by the underlying support.

Keywords Supported model catalysts · NSR catalysts · Barium oxide · Nitrogen dioxide · Particle size effects · IR reflection absorption spectroscopy · Scanning tunneling microscopy

Tailoring selectivity and activity of catalyst materials by controlled nanostructuring is a future vision in heterogeneous catalysis. At the purely empirical level, catalyst structures are optimized by varying preparation procedures and conditions, however, from a fundamental point of view, the underlying effects, which control the reaction kinetics and, therefore, the catalytic performance are poorly understood [1, 2].

It is well accepted that for many catalytic reaction systems the size of the catalysts particles is a critical parameter. Traditionally, size effects have been mainly discussed in connection with catalytically active metal particles (see e.g. [3, 4]). In recent works, ionic nanoparticles (mainly oxides) also showed pronounced size dependent effects as well, although the physical origins of these effects may be entirely different [5, 6]. In this study, we present evidence for an extremely prominent size effect on a nanostructured ionic catalyst surface, affecting both kinetics and thermodynamics. Scrutinizing a model system for NO_x storage and reduction (NSR) catalysis, we show that with decreasing particle size, the transformation of BaO nanoparticles into $Ba(NO_3)_2$ becomes increasingly efficient, whereas on the other hand, the thermal stability of the $Ba(NO_3)_2$ decreases drastically.

NSR catalysis represent one possible concept for reduction of NO_x exhaust streams produced under lean-burn conditions [7, 8]. Lean-burn engines, i.e. combustion engines which are operated under air-rich condition, have

---

A. Desikusumastuti · M. Laurin · M. Happel · J. Libuda (✉)
Lehrstuhl für Physikalische Chemie II, Universität Erlangen-Nürnberg, Egerlandstr. 3, 91058 Erlangen, Germany
e-mail: libuda@chemie.uni-erlangen.de

Present Address:
M. Laurin
Research Centre for Spectrochemistry, The University of Tokyo, Hongo, Tokyo 113-0033, Japan

Z. Qin · S. Shaikhutdinov
Fritz-Haber-Institut der Max-Planck-Gesellschaft, Faradayweg 4-6, 14195 Berlin, Germany

substantially better fuel and CO_2 efficiency, however, they may generate problems with respect to the emission of toxic gases, in particular NO_x. From a chemical point of view, it is easy to conceive that it is inherently difficult to catalytically reduce NO_x in the strongly oxidizing exhaust gas environment of a lean-burn engine. The NSR concept circumvents the problem by storing NO_x in form of $Ba(NO_3)_2$ during lean operation periods, followed by release and reduction of NO_x during short fuel-rich operation cycles. Although first commercial applications for spark-ignition engines have been successful and applications for diesel engines are planned, today's NSR catalysts still suffer from numerous shortcomings. These include for example the limited possibilities of tuning the temperature windows for NO_x storage and release, the low storage efficiency, the limited thermal stability of the NSR catalysts, as well as deactivation and poisoning [9].

Unfortunately, the elementary processes in NSR catalysis are poorly understood at the microscopic level, largely preventing the development of rational and directed strategies towards improvement. While the NSR concept has attracted considerable attention in applied catalysis (see e.g. [8, 10–12]), model studies using a surface science type approach are in their very infancy. However, Bowker and coworkers [13, 14] as well as Ozensoy et al. [15] have recently shown that the related model surfaces and reactions can indeed be studied in an ultrahigh vacuum (UHV) environment.

In the present work, we take advantage of the full potential of the surface-science-based model catalyst approach, which allows application of a broad spectrum of experimental techniques, providing detailed structural and chemical information [16]. Nanostructured BaO/Al_2O_3 model systems are prepared under UHV conditions and characterized with respect to their structure and morphology using scanning tunneling microscopy (STM). The formation and decomposition kinetics of $Ba(NO_3)_2$ is monitored using in-situ IR reflection absorption spectroscopy (IRAS) in combination with molecular beam (MB) techniques [17]. It is shown that both the formation and the decomposition of $Ba(NO_3)_2$ are subject to very strong particle size dependent effects.

MB/IRAS experiments were performed in an UHV apparatus at the University Erlangen-Nuremberg, which allows up to four effusive beams and a supersonic beam to be superimposed on the sample. Additionally, the system is equipped with a FTIR spectrometer (Bruker IFS66/v), a beam monitor which allows alignment and intensity calibration of the beams, two quadrupole mass spectrometers, a vacuum transfer system with high pressure cell and all necessary preparation tools. The NO_2 beam (Linde, 99.0%) was generated from an effusive beam doser and modulated by a valve system. All measurements were performed by remote controlled sequences, exposing the sample to pulses of NO_2 at variable beam intensities between $2.7 \times 10^{13}\ cm^{-2}\ s^{-1}$ (equivalent pressure: 1.2×10^{-7} mbar) and $3.2 \times 10^{15}\ cm^{-2}\ s^{-1}$ (equivalent pressure 1.4×10^{-5} mbar), followed by acquisition of IR spectra. In annealing experiments, difference spectra were taken at 300 K with the sample being successively heated to the pre-set temperature with heating rates of about $3\ Ks^{-1}$. IR spectra were acquired at a spectral resolution of $2\ cm^{-1}$ with typical acquisition times of 38 s.

STM measurements (Micro H, Omicron) were performed in a separate UHV chamber at the Fritz-Haber-Institute, Berlin). The chamber is equipped with standard sample cleaning/preparation facilities. All images were recorded using commercial Pt/Ir tips (L.O.T.-Oriel GmbH) with tunneling parameters (bias and current) as follows: Fig. 1, A: +3.0 V, 0.15 nA; B: +2.67 V, 0.16 nA; C: +2.27 V, 0.17 nA; D: +2.5 V, 0.17 nA; Fig. 2, A: +2.7 V, 0.16 nA; B: +2.6 V, 0.18 nA.

For preparation of the model surfaces, a NiAl(110) surface was cleaned by numerous cycles of sputtering and vacuum annealing, followed by two cycles of oxidation in 10^{-6} mbar O_2 at 550 K and UHV annealing at 1135 K in order to prepare the Al_2O_3 film on NiAl(110). With respect to the details of the procedure we refer to the literature [18]. The quality of the film was checked by LEED, and complete oxidation of the surface was proven by the absence of CO adsorption at 100 K.

For the preparation of the BaO particles, we proceeded as follows: First, the Ba metal was manually cleaned under inert gas atmosphere (glove box) and placed into a Mo crucible. In order to prevent oxidation, the crucible filled with Ba was covered with decane before it was mounted in a commercial electron beam assisted evaporator (Focus EFM3). The evaporator was installed into the UHV chamber immediately before pumping out. Under UHV conditions, the Ba source was calibrated using a quartz microbalance. During deposition the sample was biased to the same potential as the Ba source in order to avoid surface defect generation by Ba ion bombardment. Ba was deposited at 300 K at typical rates of $1.0 \times 10^{13}\ atoms \cdot cm^{-2} \cdot s^{-1}$ (an average film thickness of 1 Å Ba corresponds to $1.6 \times 10^{14}\ atoms \cdot cm^{-2}$) and subsequently oxidized by exposure to 6×10^{-7} mbar O_2 for 90 s in the "$(BaO)_{\sim 30}$" preparation and for 900 s in the "$(BaO)_{\sim 600}$" preparation.

In Fig. 1 we illustrate the preparation procedure for the BaO/Al_2O_3 model surface. As an oxide support, we use an ordered and atomically flat Al_2O_3 film on NiAl(110) [18], which has been applied as a model support in numerous studies (see e.g. [17, 19–21]). Recently, a detailed structure model of the surface has been suggested by Kresse et al. [22]. In Fig. 1a we show an STM image and a schematic representation of the system following this model (domain

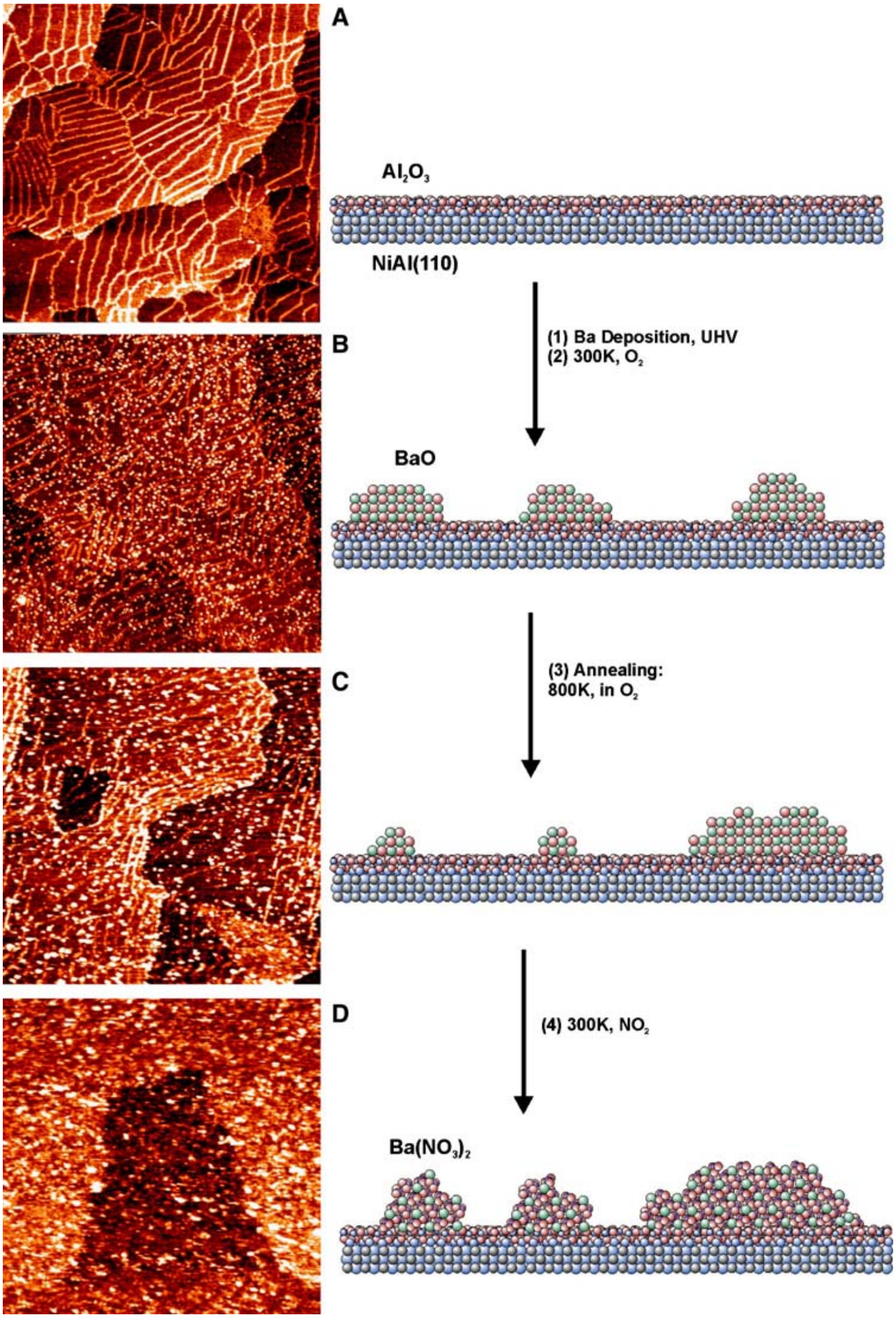

Fig. 1 STM images ($300 \times 300\ nm^2$) and schematical representations illustrating the preparation steps of the NO_x storage model catalyst: (**a**) Al_2O_3/NiAl(110): ordered and atomically flat alumina model support, (**b**) BaO/Al_2O_3/NiAl(110): BaO nanoparticles prepared by Ba deposition in UHV (1.6×10^{14} atoms cm^{-2}) and subsequent oxidation by of O_2 (6×10^{-7} mbar) at 300 K, (**c**) BaO/Al_2O_3/NiAl(110), annealed: the sample (**b**) after annealing in O_2 (10^{-7} mbar) to 800 K, (**d**) $Ba(NO_3)_2/Al_2O_3$/NiAl(110): the sample (**c**) after extended exposure to NO_2 (approximately 6000 L at 300 K, 1 L (Langmuir) corresponds to a gas dose of 10^{-6} Torr·s)

boundaries between oxide domains are visible as bright lines). In the next step, Ba is deposited under UHV conditions, followed by exposure to oxygen at 300 K in order to form BaO nanoparticles (Fig. 1b). The corresponding STM image shows a high nucleation density and a relatively homogeneous distribution of particles on the surface. Based on previous work, we may be expect different processes to be activated upon annealing, including particle ripening, mixing with the Al_2O_3 support, diffusion through the support [19] and, finally, decomposition of potentially formed BaO_2 species [23]. In order to test the potential influence of these effects on the reactivity with respect to NO_2, the BaO/Al_2O_3 model surface is annealed to 800 K in O_2 (10^{-7} mbar) and again characterized by STM at room temperature (see Fig. 1c). It is observed that the particle density is subject to moderate decrease only, whereas the width of the particle size distribution increases substantially (particle density before annealing: $(5.0 \pm 1.0) \times$

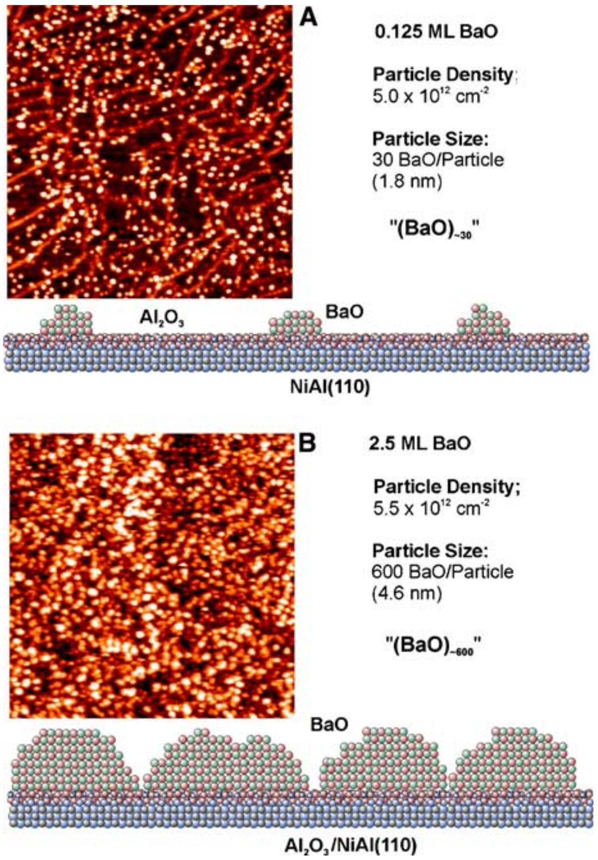

Fig. 2 STM figures and schematical representations NO_x storage model catalysts with two average sizes of BaO nanoparticles (all STM figures: 150 nm × 150 nm, see text for details): (**a**) $(BaO)_{\sim 60}/Al_2O_3/NiAl(110)$: small BaO nanoparticles prepared by deposition of low amounts of BaO (**b**) $(BaO)_{\sim 1100}/Al_2O_3/NiAl(110)$: larger BaO nanoparticles formed at high coverage of BaO

10^{12} cm^{-2}; after annealing: $(3.3 \pm 1.0) \times 10^{12}$ cm^{-2}). It is concluded that annealing leads to sintering of the particles most probably via Ostwald ripening and coalescence, whereas mixing and loss of BaO by diffusion into and through the Al_2O_3 film occurs to a minor extent only. In a final step the BaO/Al_2O_3 surface is exposed to NO_2 using a MB or directional gas doser in the STM chamber (see Fig. 1d). It is found that both the roughness of the surface and the average particle size increase significantly, whereas the particle density is largely conserved. This behavior is expected upon transformation of individual BaO particles into $Ba(NO_3)_2$, due to the larger molar volume of the latter compound (BaO: rock salt structure, lattice constant a = 5.54 Å, see [24], $V_{m,BaO} = 26.9$ cm^3 mol^{-1}; $Ba(NO_3)_2$: cubic structure, fcc lattice of Ba^{2+} ions, lattice constant 8.12 Å, see [25],$V_{m,Ba(NO_3)_2} = 80.7$ cm^3 mol^{-1}).

Once the nucleation and growth behavior is characterized, the BaO particle size can be varied via the amount of Ba deposited. Specifically, we consider two situations:

(1) "$(BaO)_{\sim 30}$": Figure 2a shows an STM image after deposition of a sub-monolayer (ML) equivalent of metallic Ba (1.6×10^{14} atoms cm^{-2}) and subsequent transformation into BaO. The average coverage corresponds to 0.125 ML of BaO, defining 1 ML BaO as a double layer of Ba^{2+} and O^{2-} ions with the bulk lattice constant (see above). Again, STM reveals the formation of a relatively homogeneous distribution of three-dimensional islands, with no strong preferential nucleation at line defects such as domain boundaries and steps (compare e.g. [19]). The particle density is determined as $(5.0 \pm 1.0) \times 10^{12}$ particles cm^{-2}, yielding an average aggregate size of $(BaO)_{\sim 30}$ or an average particle diameter of 1.8 nm assuming aggregates with hemispherical morphology.

(2) "$(BaO)_{\sim 600}$": Figure 2b shows a corresponding STM image after deposition of a multilayer equivalent of metallic Ba (3.2×10^{15} atoms cm^{-2}) and subsequent transformation into BaO. The average film thickness corresponds to 2.5 monolayers of BaO (see above). STM shows larger three-dimensional islands, again exhibiting a relatively homogeneous distribution. No BaO free Al_2O_3 surface is detectable by STM. With $(5.6 \pm 1.0) \times 10^{12}$ particles cm^{-2}, the particles density is only slightly higher than in case of the lower coverage situation. This behavior is typical for particle growth on oxide supports [19, 26], and shows that after initial nucleation at low coverage, further deposition mainly leads to particle growth, before at very high exposure coalescence becomes dominant. Using above values, we calculate an average aggregate size of $(BaO)_{\sim 600}$, corresponding to a particle diameter of 4.6 nm (again assuming hemispherical particle morphology).

In the next step, we examine the reactivity of the supported BaO particles as a function of particle size. For this purpose, the BaO/Al_2O_3 model surface is exposed to series of NO_2 pulses using a MB doser, each pulse followed by acquisition of IR spectra in a fully remote controlled sequence. Selected spectra of the v(N–O) stretching frequency region after large NO_2 exposure are displayed in Fig. 3. The development of the integral intensity of the bands in the NO stretching frequency region as a function of exposure is shown in the inset.

We focus on the small $(BaO)_{\sim 30}$ particles first (Fig. 3a). Four bands develop as a function of NO_2 exposure at 1331 cm^{-1} (1), 1465 cm^{-1} (2), 1588 cm^{-1} (5), and 1645 cm^{-1} (6). By comparison with spectra on the clean Al_2O_3 support (not shown), the bands (5) and (6) can be attributed to a surface nitrate species on Al_2O_3. A possible assignment is to bridging or chelating bidentate surface nitrates (see e.g. [27–29]. Bands (1) and (2) are related to

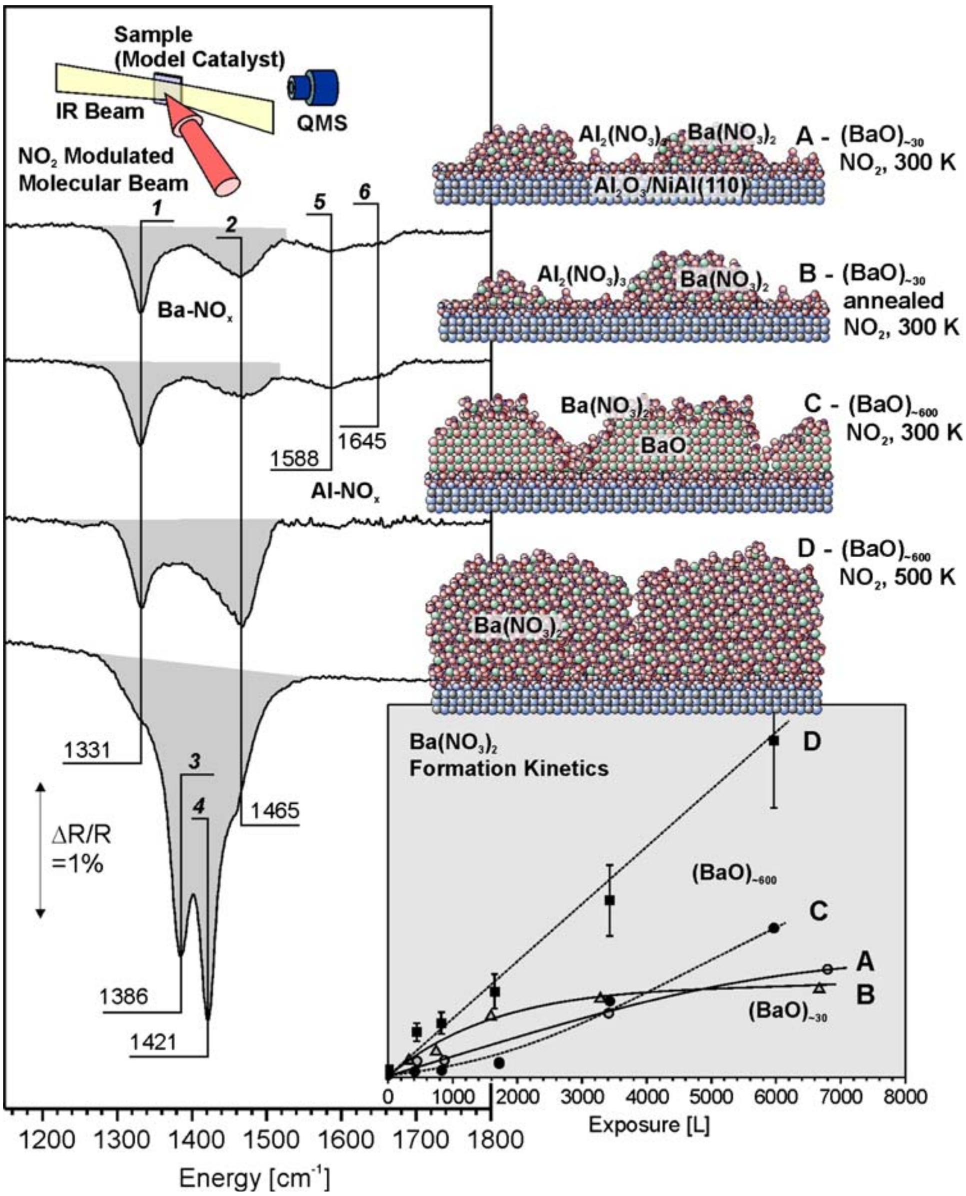

Fig. 3 Interaction of NO$_2$ with a NO$_x$ storage model catalysts as a function of BaO particle size. IR spectra of the NO stretching frequency region after extended exposure to NO$_2$: (**a**) (BaO)$_{\sim60}$/Al$_2$O$_3$/NiAl(110), $\sim$6700 L NO$_2$ at 300 K; (**b**) (BaO)$_{\sim60}$/Al$_2$O$_3$/NiAl(110), annealed, $\sim$6700 L NO$_2$ at 300 K; (**c**) (BaO)$_{\sim1100}$/Al$_2$O$_3$/NiAl(110), $\sim$6000 L NO$_2$ at 300 K; (**d**) (BaO)$_{\sim1100}$/Al$_2$O$_3$/NiAl(110), $\sim$6000 L NO$_2$ at 500 K. The inset shows the integral absorption in the NO stretching frequency region as a function of NO$_2$ exposure (1 L (Langmuir) corresponds to a gas dose of 10^{-6} Torr·s)

surface nitrate on the BaO particles. On the basis of the exposure and size dependent behavior it is concluded that the bands are surface-related with at least two different species contributing. Based on the literature, the straightforward assignment would be to monodentate nitrates [27–32]. An unambiguous assignment appears difficult, however, due to the complexity of NO related surface chemistry, showing a wealth of different surface species with partially overlapping bands (see e.g. [33]). As we will be discussed in a forthcoming publication, the most probable assignment is in fact to a combination of monodentate and bidentate surface nitrates [34].

It should be pointed out that a quantitative interpretation of IRAS is complicated by the metal surface selection rule, MSSR, and dipole coupling effects, see e.g. [35]. For example, the characteristic nitrite band in the range from 1200 to 1250 cm^{-1} may be attenuated due to the MSSR. Therefore, we restrict ourselves to qualitative considerations, in the following.

Comparing the spectra for NO$_2$ on (BaO)$_{\sim30}$ at 300 K without (Fig. 3a) and with (Fig. 3b) pre-annealing, a nearly identical behavior is found. This indicates that thermal treatment, possibly leading to enhanced interaction of BaO with the alumina support, does not substantially alter the chemical behavior with respect to NO$_2$. The only differences between the two situations are the slightly higher rate of Ba(NO$_3$)$_2$ formation and the somewhat lower band intensities at saturation for the non-annealed sample. This observation also supports the STM based conclusion on minor BaO/support intermixing.

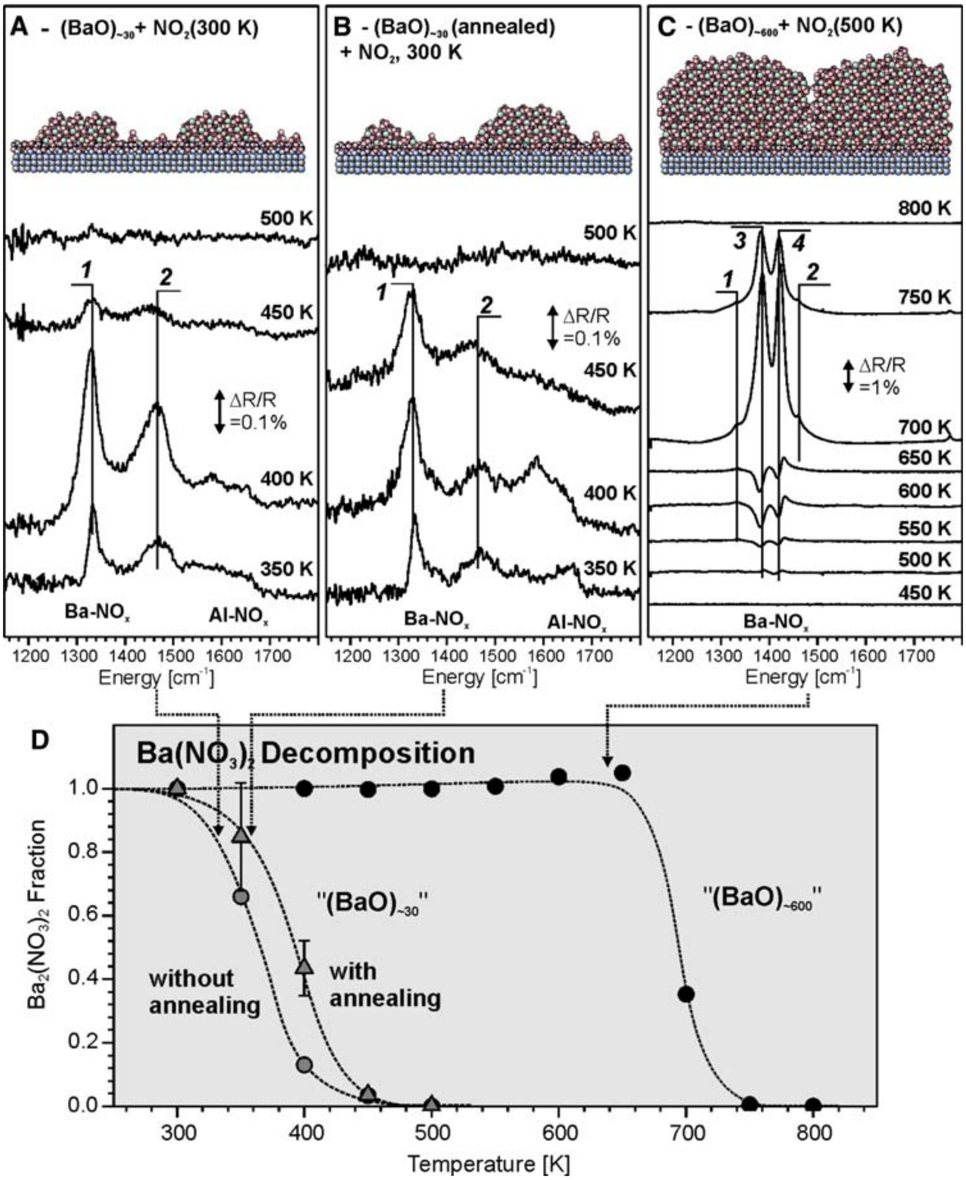

Fig. 4 Thermal decomposition of surface and bulk nitrate species on a NO_x storage model catalysts as a function of BaO particle size. The IR difference spectra of the NO stretching frequency region were acquired at 300 K (see text for details). The upper panels correspond to decomposition nitrates formed from (**a**) $(BaO)_{\sim 30}/Al_2O_3/$NiAl(110) (~6700 L NO_2 at 300 K), (**b**) $(BaO)_{\sim 30}/Al_2O_3/$NiAl(110), after annealing at 800 K in O_2 (~6700 L NO_2 at 300 K); (**c**) $(BaO)_{\sim 600}/Al_2O_3/$NiAl(110), (~6000 L NO_2 at 500 K). The lower panel (**d**) shows the normalized integral absorption in the NO stretching frequency region as a function of annealing temperature as extracted from the IRAS data in (**a**) to (**c**)

We now shift our attention to the large $(BaO)_{\sim 600}$ particles. Upon interaction with NO_2 at 300 K, the bands (1) and (2) appear successively. Initial band intensities are lower than that for the $(BaO)_{\sim 30}$, indicating slower nitrate formation. This finding and the absence of bulk nitrate bands suggests that the reaction is kinetically limited. In order to validate this hypothesis, the reaction with NO_2 is performed at 500 K (D). Two very strong bands appear at 1386 cm^{-1} (3) and 1421 cm^{-1} (4), which continuously grow in intensity as a function of NO_2 exposure. These bands can be assigned to ν_{as} of ionic NO_3^- of bulk $Ba(NO_3)_2$ (compare [27, 28, 32, 33]). Thus, it is concluded that under these conditions multilayer $Ba(NO_3)_2$ formation occurs, which may eventually lead to complete transformation of the $(BaO)_{\sim 600}$ particles into nitrates. It should be noted that in spite of the dominance of the bulk bands the surface NO_x species (bands (1) and (2)), remain visible as a shoulder.

Finally, we come to the most relevant question from the point of view of application, which is the influence of the particle size on the thermal stability of the NO_x species. In order to explore this point, the NSR model systems were annealed, following decomposition via IRAS (see Fig. 4, please note that *difference* spectra between successive heating cycles are displayed. Accordingly, the positive signals indicate the decomposition of nitrates/nitrites species upon heating to elevated temperatures).

First we investigate the $(BaO)_{\sim 600}/Al_2O_3$ after multilayer nitrate formation (Fig 4c). No spectral changes can be detected below 500 K. In the region between 500 and 650 K weak features are observed in the spectral regions of bands (3) and (4), as a result of a slight blue shift of the bands without significant change of their integral intensity (see Fig. 4d). In the temperature region between 700 and 750 K, however, strong decomposition features ($\Delta R/R > 0$) appear in the spectral region of all Ba-related ν(N–O) bands (1,2,3,4). No further bands appear in the difference spectra at temperatures above 750 K. It is concluded that below 700 K the $Ba(NO_3)_2$ particles are essentially stable with only a minor degree of thermally activated restructuring. At 700 K decomposition of the $Ba(NO_3)_2$ phase occurs, which is in accordance with studies on NSR powder catalysts ([28], see also [8]). The most important observation concerns the decomposition of the surface related NO_x species (band (1) and (2)). It is concluded that decomposition of these species occurs in the same temperature interval as the bulk phase, i.e. at temperatures around 700 K.

Corresponding IRAS spectra for successive annealing of the small nitrate/nitrite particles generated from $(BaO)_{\sim 30}$ are shown in Fig. 4a and b. In comparison with the large particles, a very different behavior is observed. Decomposition features in the region of both surface related bands (1) and (2) appear in the temperature region between 350 and 450 K (decomposition of surface nitrates on Al_2O_3 gives rise to additional weaker features at higher frequency). This is in sharp contrast to the large particles, for which the corresponding surface species show a much higher stability. Indeed, the surface nitrate species on the large particles decompose at the same temperature as the bulk features, i.e. at 700 K.

There are two groups of effects which may contribute to the size dependent stability of surface NO_x species. (i) The first group is related to the *reduced electrostatic potential* of a small ionic particle, which may give rise to particle size dependent formation and activation energies. For small BaO clusters, this contribution has recently been investigated theoretically by Grönbeck et al. [36]. A moderate size dependence was predicted, which may contribute, but is unlikely to be the only source of the effect observed here. (ii) Secondly, we have to take into account the *interaction with the underlying support*. For the small particles surface nitrates/nitrites are the dominating NO_x storage species. The stability of these surface species is expected to depend critically on the underlying support. For monodisperse BaO_n clusters, the interaction with the Al_2O_3 support was recently suggested to have a stabilizing influence on NO_2 adsorption [37]. Indeed, activating an enhanced interaction with the Al_2O_3 by pre-annealing the $(BaO)_{\sim 30}/Al_2O_3$ leads to a slight increase of the decomposition temperature (see Fig. 4b). However, this effect cannot explain the low stability of surface NO_x on small BaO particles. We have to conclude that the surface NO_x species in close contact with the Al_2O_3 are strongly destabilized in comparison with the corresponding surface species on large nanoparticles terminated by Ba oxide and Ba nitrate multilayers.

In summary, we have obtained precise correlations between structural properties of a nanostructured NO_x storage material and its reactivity by using a single-crystal-based model catalyst approach. For BaO particles on Al_2O_3 we present evidence for strong particle size dependent effects with respect to the formation and decomposition of surface-related $BaNO_x$ species. The decomposition temperature can be tuned over an exceptionally large temperature interval by changing the BaO particle size. This result may be helpful with respect to the optimization of NO_x storage properties and the interpretation of deactivation processes, which hamper commercial applications of NSR catalysts.

Acknowledgment This project was supported by the Umicore AG & Co KG (Automotive Catalysts). Financial support by the following organizations is acknowledged: Deutsche Forschungsgemeinschaft (DFG), EU (COST D-41), Fonds of the Chemical Industry (FCI), Deutscher Akademischer Austauschdienst (DAAD), Zerweck Fonds (University Erlangen-Nuremberg). The authors thank Hans-Joachim Freund (FHI Berlin) for supporting the STM measurements. We thank Herbert Pfnür (University Hannover) for helpful comments concerning the deposition of barium and Karsten Meyer, Matthias Moll, Marc Gärtner and Carola Vogel (University Erlangen) as well as Friederike Jentoft and Robert Schlögl (FHI, Berlin) for the possibility to use their local glove box facilities.

References

1. Ertl G, Knoezinger H, Weitkamp J (eds) (1997) Handbook of heterogeneous catalysis. VCH, Weinheim
2. Chorkendorff I, Niementsverdriet JW (2003) Concepts of modern catalysis and kinetics. Wiley-VCH, Weinheim
3. Bond BC (1985) Surf Sci 156:966
4. Haruta M (1997) Catal Today 36:153
5. Stankic S, Müller M, Diwald O, Sterrer M, Knözinger E, Bernardi J (2005) Angew Chem Int Ed 44:4917
6. Sterrer M, Yulikov M, Fischbach E, Heyde M, Rust HP, Pacchioni G, Risse T, Freund H-J (2006) Angew Chem Int Ed 45:2630
7. Takahashi N, Shinjoh H, Iijima T, Suzuki H, Yamazaki K, Yokota K, Suzuki H, Miyoshi N, Matsumoto S, Tanizawa T, Tanaka T, Tateishi S, Kashahara K (1996) Catal Today 27:63
8. Epling WS, Campbell LE, Yezerets A, Currier NW, Parks JE II (2004) Catal Rev 46:163
9. Rohr F, Göbel U, Kattwinkel P, Kreuzer T, Müller W, Philipp S, Gélin P (2007) Appl Catal B 70:189
10. Fridell E, Skoglundh M, Westerberg B, Johansson S, Smedler G (1999) J Catal 183:196
11. Fridell E, Amberntsson A, Olsson L, Grant AW, Skoglundh M (2004) Top Catal 30/31:143
12. Sedlmair C, Seshan K, Jentys A, Lercher JA (2003) J Catal 214:308
13. Stone P, Ishii M, Bowker M (2003) Surf Sci 537:179
14. Tsami A, Grillo F, Bowker M, Nix RM (2006) Surf Sci 600:3403
15. Ozensoy E, Peden CHF, Szanyi J (2006) J Phys Chem B 110:17001
16. Freund H-J, Bäumer M, Libuda J, Risse T, Rupprechter G, Shaikhutdinov S (2003) J Catal 216:223

17. Libuda J, Freund H-J (2005) Surf Sci Rep 57:157
18. Jaeger RM, Kuhlenbeck H, Freund H-J, Wuttig M, Hoffmann W, Franchy R, Ibach H (1991) Surf Sci 259:235
19. Bäumer M, Freund H-J (1999) Prog Surf Sci 61:127
20. Schauermann S, Hoffmann J, Johánek V, Hartmann J, Libuda J, Freund H-J (2002) Angew Chem Int Ed 41:2532
21. Johanek V, Schauermann S, Laurin M, Libuda J, Freund H-J (2003) Angew Chem Int Ed 42:3035
22. Kresse G, Schmid M, Napetschnig E, Shishkin M, Kohler L, Varga P (2005) Science 308:1440
23. Ozensoy E, Peden CHF, Szanyi J (2006) J Phys Chem B 110:17009
24. Zollweg RJ (1955) Phys Rev 100:671
25. Nowotny H, Heger G (1982) Acta Cryst C 39:952
26. Henry CR (1998) Surf Sci Rep 31:231
27. Prinetto F, Ghiotti G, Nova I, Lietti L, Tronconi E, Forzatti P (2001) J Phys Chem B 105:12732
28. Westerberg B, Fridell E (2001) J Mol Catal A – Chem 165:249
29. Sedlmair C, Seshan K, Jentys A, Lercher JA (2002) Catal Today 75:413
30. Nova I, Castoldi L, Prinetto F, Santo VD, Lietti L, Tronconi E, Forzatti P, Ghiotti G, Psaro R, Recchia S (2004) Top Catal 30/31:181
31. Broquist P, Grönbeck H, Fridell E, Panas I (2004) J Phys Chem B 108:3523
32. Szailer T, Kwak JH, Kim DH, Hanson JC, Peden CHF, Szanyi J (2006) J Catal 239:51
33. Hadjiivanov KI (2000) Catal Rev – Sci Eng 42:71
34. Desikusumastuti A, Happel M, Laurin M, Libuda J (in preparation)
35. Hoffmann FM (1983) Surf Sci Rep 3:107
36. Grönbeck H, Broquist P, Panas I (2006) Surf Sci 600:403
37. Cheng L, Ge Q (2007) Surf Sci 601:L65